ADVANCED MATERIALS
www.advmat.de

Integrated Urinalysis Devices Based on Interface-Engineered Field-Effect Transistor Biosensors Incorporated With Electronic Circuits

Yanbing Yang, Jingfeng Wang, Wanting Huang, Guojia Wan, Miaomiao Xia, Duo Chen, Yun Zhang, Yiming Wang, Fuding Guo, Jie Tan, Huageng Liang, Bo Du, Lilei Yu,* Weihong Tan, Xiangfeng Duan, and Quan Yuan**

Urinalysis is attractive in non-invasive early diagnosis of bladder cancer compared with clinical gold standard cystoscopy. However, the trace bladder tumor biomarkers in urine and the particularly complex urine environment pose significant challenges for urinalysis. Here, a clinically adoptable urinalysis device that integrates molecular-specificity indium gallium zinc oxide field-effect transistor (IGZO FET) biosensor arrays, a device control panel, and an internet terminal for directly analyzing five bladder-tumor-associated proteins in clinical urine samples, is reported for bladder cancer diagnosis and classification. The IGZO FET biosensors with engineered sensing interfaces provide high sensitivity and selectivity for identification of trace proteins in the complex urine environment. Integrating with a machine-learning algorithm, this device can identify bladder cancer with an accuracy of 95.0% in a cohort of 197 patients and 75 non-bladder cancer individuals, distinguishing cancer stages with an overall accuracy of 90.0% and assessing bladder cancer recurrence after surgical treatment. The non-invasive urinalysis device defines a robust technology for remote healthcare and personalized medicine.

1. Introduction

Bladder cancer (BC) is one of the most common and aggressive malignant tumors in the human urinary system with the increasing trend of morbidity and mortality worldwide.[1–4] The characteristics of complex pathologic patterns, the lack of obvious specific clinical symptoms, and high postoperative recurrence of BC require more efficient diagnosis and prognosis of BC.[5,6] Current clinical gold standard cystoscopy for BC diagnosis relies on the insertion of an optical endoscope into the bladder cavity through urethra to image the suspected lesions.[7,8] This process is highly invasive and would cause urethra and bladder injury, resulting in hematuria and even urinary bacterial infection within a few days after examinations.[9] Critically, cystoscopy diagnosis is plagued with the inherent bladder tumor heterogeneity, and therefore, limits the accuracy of early BC diagnosis.[10] Recently, noninvasive liquid biopsy emerges as an alternative to address the bottleneck of spatiotemporal tumor heterogeneity and to obtain disease-relevant molecular information for clinical cancer diagnosis and cancer status monitoring.[11–20]

Bladder is a urine storage organ that has been recognized as the metabolic microenvironment for bladder tumor cells, and its carcinogenesis and progression could make a pivotal impact on urine.[21] In this regard, the development of a urine biopsy provides a powerful strategy toward noninvasive early diagnosis and prognosis of BC. Clinically, urinalysis has been routinely utilized to detect abnormal metabolic biomarkers in urine for the assessment of health status and preliminary screening of diseases.[22–25] However, the physiologically relevant biomarkers detected by routine urinalysis are generally limited to high concentration targets over the micromolar level. On the other hand, the concentration

Y. Yang, J. Wang, W. Huang, G. Wan, M. Xia, D. Chen, Y. Zhang, Y. Wang, F. Guo, B. Du, L. Yu, Q. Yuan
Department of Cardiology
Institute of Molecular Medicine
Renmin Hospital of Wuhan University
College of Chemistry and Molecular Sciences
School of Computer Science
Wuhan University
Wuhan 430072, China
E-mail: yangyanbing@whu.edu.cn; lileiyu@whu.edu.cn; yuanquan@whu.edu.cn

The ORCID identification number(s) for the author(s) of this article can be found under https://doi.org/10.1002/adma.202203224.

DOI: 10.1002/adma.202203224

J. Tan, W. Tan, Q. Yuan
Molecular Science and Biomedicine Laboratory (MBL)
State Key Laboratory of Chemo/Biosensing and Chemometrics
College of Chemistry and Chemical Engineering
Hunan University
Changsha 410082, China

H. Liang
Union Hospital
Tongji Medical College
Huazhong University of Science and Technology
Wuhan 430030, China

X. Duan
Department of Chemistry and Biochemistry
University of California, Los Angeles
Los Angeles, CA 90095-1569, USA

of BC-relevant biomarkers in urine is usually extremely low, which is further complicated by the deeply complex urine environment. Hence, it is highly desirable to develop a clinical utility urinalysis technique with high sensitivity to identify trace bladder tumor biomarkers in urine for efficient early-stage and accurate BC diagnosis.

Here, we report and validate an integrated urinalysis device that is composed of an indium gallium zinc oxide field-effect transistor (IGZO FET) biosensor array, a device control unit, and an Internet terminal to afford direct analysis of bladder-tumor-associated proteins in untreated urine samples. In this urinalysis device, molecular-specificity IGZO FET sensing array units with engineered interfaces and high uniformity enable the simultaneous and reliable monitoring of five bladder-tumor-associated protein molecules in urine samples, significantly improving the diagnostic accuracy. The device control panel with data conversion and wireless communication ability permit the real-time transmission of bladder-tumor-associated protein signatures to the Internet terminal, which is further analyzed through machine-learning algorithm. Overall, our technology delivers a 95.0% accuracy in identifying BC after analyzing the protein signatures in a cohort of urine samples from 197 BC patients and 75 non-BC individuals. Importantly, the integrated urinalysis device could distinguish among stage I–III cancer stages in BC patients with an accuracy of higher than 90.0% and is effective in monitoring the status of patients in vivo to enable the prognosis and guide the therapy. This integrated urinalysis device performs the capability to real-time track the progression, metastatic and recurrence of BC as well as provide an efficient monitoring platform to promote the development of personalized health management.

2. Results and Discussion

2.1. Assay Validation

The IGZO FET devices were fabricated on a Si/SiO_2 substrate by photolithography in which Au source and drain electrodes were deposited by thermal evaporation, and the magnetic sputter-deposited IGZO layer with a thickness of 25 nm served as channel material (Figure S1, Supporting Information). The efficient biosensing relies first on the electrical performance of IGZO FET device. As indicated in Figure S2, Supporting Information, the transfer characteristic of back-gated IGZO FET shows n-type transistor behavior with an on-state current of 40 μA, current on/off ratio of 1×10^6, and carrier mobility (μ_{FE}) of 15.8 $cm^2\ V^{-1}\ s^{-1}$, and these electronic properties are comparable to that of previously reported works (Table S1, Supporting Information).[26,27] In addition, the transfer/output characteristics of IGZO FET device were well maintained under liquid-gated voltage, promising the extraordinary performance of IGZO FET in biosensing (Figure S3, Supporting Information). To identify bladder-tumor-relevant proteins in urine samples, a specific recognition molecule such as antibody should be functionalized on the IGZO FET device to achieve a biosensor (**Figure 1**a). In the biosensing process, the binding of charged target proteins with recognition molecules would induce the accumulation or depletion of carriers in the IGZO channel and generate a change in current amplitude (Figure 1b).

In biological buffer solutions, the charged protein molecules would be surrounded by oppositely charged ions due to electrostatic interaction, thus decreasing the effective charge of proteins.[28–41] This effect is known as Debye screening, and due to the Debye screening effect, the effective electrical field of FET biosensors could only be controlled within a distance called the Debye length (λ_D):[42,43]

$$\lambda_D = \sqrt{\frac{\varepsilon k_B T}{2 N_A q^2 I}} \tag{1}$$

where ε is the dielectric constant of electrolyte. k_B, T, and N_A represent the Boltzmann's constant, temperature, and Avogadro's number, respectively. I is the ionic strength of the solution. q is the elementary charge. According to this equation, it is definite that λ_D is inversely proportional to ionic strength, and the value of λ_D narrows from 7.0 to 0.7 nm when the concentration of phosphate-buffered saline (PBS) solution increases from 0.1 to 10×10^{-3} M (Figure 1b).

In urine samples with extremely high ionic strength, the surface charge of proteins would be severely screened. To overcome this limitation, the arrangements of recognition molecules on the IGZO surface were regulated to minimize its occupied length for the purpose of narrowing the distance between target protein molecules and IGZO channel. Specifically, two different immobilization strategies that could bind different terminals of antibodies for bladder-tumor-specific nuclear matrix protein 22 (anti-NMP22) were utilized to regulate antibody arrangements on IGZO (Figure 1a). The IGZO surface was first modified with (3-aminopropyl) triethoxysilane (APTES) to introduce amino groups. Subsequently, anti-NMP22 was separately immobilized on the IGZO surface by coupling to N-terminal with the assistance of glutaraldehyde or C-terminal through 1-ethyl-3-(3-dimethylaminopropyl) carbodiimide hydrochloride and N-hydroxysulfosuccinimide (EDC/NHS) chemistry. The presence of absorption peaks (1530 and 1650 cm^{-1}) that corresponded to amide bonds in the attenuated total reflection flourier transformed infrared spectroscopy (ATR-FTIR) curves as well as the appearance of characteristic peaks for C 1 s (286.6 eV), N 1 s (399.9 eV), and S 2p (162.4 eV) in the X-ray photoelectron spectra (XPS) curves of N-terminal functionalized anti-NMP22/IGZO, suggesting that anti-NMP22 was successfully immobilized on the IGZO surface (Figures S4 and S5, Supporting Information). As the pKa of amine groups at N-terminus is lower than 7.4 and the pKa of amine groups at side chains is higher than 7.4, a pH of 7.4 was used to ensure that the N-terminus of antibody is deprotonated and reactive to glutaraldehyde, while the side-chain amines are protonated and unable to react with glutaraldehyde. Consequently, the arrangement of antibodies on N-terminal functionalized IGZO biosensor is relatively uniform. By contrast, as the non-selective EDC/NHS chemistry would allow the conjugation of both C-terminus and side chain carboxyl groups, the arrangement of anti-NMP22 on C-terminal functionalized IGZO is relatively random. This is as confirmed by the increased surface roughness of C-terminal functionalized IGZO compared with that of N-terminal

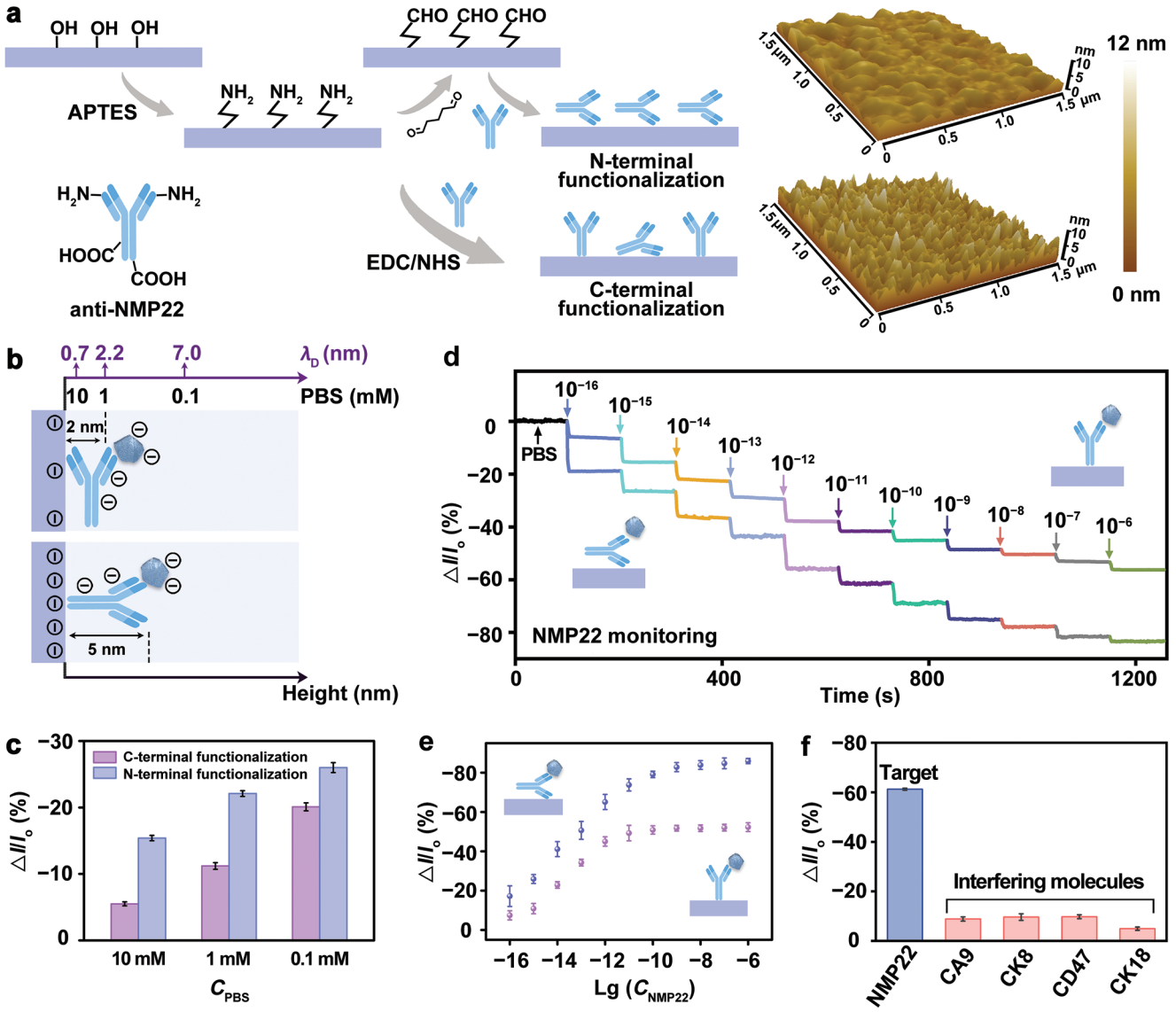

Figure 1. Interface engineering of FET biosensor. a) Schematic and AFM images of anti-NMP22 functionalized on the IGZO device by N-terminal (top) and C-terminal (bottom). b) Debye lengths of PBS buffer and protein height. The sensing mechanism of the IGZO FET biosensor was also plotted. c) Current response of N-terminal and C-terminal functionalized anti-NMP22/IGZO FET biosensor toward NMP22 target under different ionic strengths. The concentration of NMP22 is 10^{-16} g mL^{-1}. d) Real-time current response of N-terminal and C-terminal functionalized anti-NMP22/IGZO FET biosensor toward NMP22 with concentrations ranging from 10^{-16} to 10^{-6} g mL^{-1}. e) Calibrated curves of N-terminal and C-terminal functionalized IGZO FET biosensors. The relationship between current response and logarithm of NMP22 concentration was plotted. The linear range of N-terminal and C-terminal functionalized anti-NMP22/IGZO biosensor is 10^{-16} to 10^{-12} g mL^{-1} and 10^{-15} to 10^{-12} g mL^{-1}, respectively. f) Selectivity of N-terminal functionalized anti-NMP22/IGZO FET biosensor. The concentrations of target protein and interfering molecules are all 10^{-12} g mL^{-1}. All the error bars represent the standard deviations of three measurements.

functionalization in the atomic force microscopy (AFM) images (Figure 1a). More importantly, the height of N-terminal and C-terminal functionalized anti-NMP22 measured with AFM are ≈2–4 nm and ≈5–7 nm (Figures S6 and S7, Supporting Information), and the average thickness of N-terminal and C-terminal functionalized antibody layer on the IGZO surface achieved by ellipsometer is ≈3.3 and 5.8 nm. These results suggest that the regulation of antibody modification sites could control antibody orientations and the occupied length of antibody on IGZO.

To investigate the antibody orientation on the biosensing performance, the N-terminal and C-terminal functionalized IGZO biosensor toward NMP22 target with a concentration of 10^{-16} g mL^{-1} under different ionic strengths was investigated. The current response ($100 \times \Delta I/I_o$) that was defined as the percentage change in I_d before and after NMP22 conjugation (ΔI) compared with I_o was recorded (Figure 1c). An optimized anti-NMP22 modification concentration and protein incubation time of 5 min were selected for the following measurements (Figures S8 and S9, Supporting Information). Figure 1c indicates that the

N-terminal functionalized IGZO FET biosensor exhibits relatively high current responses across all the investigated PBS concentrations compared with that of C-terminal functionalization. At low ions strength of 0.1×10^{-3} M PBS, the current response between N-terminal (26.0%) and C-terminal (20.0%) functionalized IGZO FET biosensor is relatively close, suggesting that the majority of charges on NMP22 target were located in the range of λ_D with a long distance of 7.0 nm. When the ionic strength increases to 1×10^{-3} M and even to 10×10^{-3} M PBS, which corresponds to λ_D of 2.2 and 0.7 nm, the current response of N-terminal functionalized IGZO FET biosensor (22.1% and 15.7% at 1×10^{-3} M and 10×10^{-3} M PBS) is significantly higher than that of C-terminal functionalization (11.1% and 5.6% at 1×10^{-3} M and 10×10^{-3} M PBS). Based on the above results, it is recognized that the regulation of antibody orientation offers an efficient strategy to minimize the occupied length of antibodies and allows the target protein to be in closer proximity to IGZO (Figure 1b). This narrowed distance would enable more charges located in the range of λ_D and improve the current response.

As the ionic strength of urine is equivalent to 10×10^{-3} M PBS, we then selected 10×10^{-3} M PBS to investigate the sensing performance of IGZO FET biosensor. As shown in Figure 1d; Figure S10, Supporting Information, the real-time current response of IGZO FET biosensor is maintained relatively stable during the whole monitoring process. In addition, the anti-NMP22 functionalized IGZO (anti-NMP22/IGZO) FET biosensor conjugated by N-terminal exhibits relatively high current response toward NMP22 across all the investigated concentrations compared to that of C-terminal functionalization (Figure 1e; Figure S11, Supporting Information). It is apparent that the anti-NMP22/IGZO FET biosensor exhibits an obvious current response of 17.2% upon the binding of NMP22 with a concentration of 10^{-16} g mL^{-1} and then exhibits a linear increase in current response as the concentration of NMP22 increases from 10^{-16} to 10^{-12} g mL^{-1}, which is boarder than that of C-terminal functionalized IGZO FET biosensor (10^{-15} to 10^{-12} g mL^{-1}). The current variation is due to the accumulation of negative surface charge in n-type IGZO channel upon the binding of negatively charged NMP22. In addition, the N-terminal and C-terminal functionalized anti-NMP22/IGZO FET biosensors all present a significantly high current response toward NMP22 target, while the current response for interfering molecules is relatively low (Figure 1f; Figure S12, Supporting Information). The detection reproducibility was investigated by measuring the transfer characteristic curves of eight anti-NMP22/IGZO FET biosensors after conjugation with NMP22 target (Figure S13, Supporting Information). As shown in Figure S13, Supporting Information, eight transfer characteristic curves are highly consistent and the calculated relative signal deviation (RSD) is 4.3%, demonstrating that the functionalized IGZO biosensors exhibit excellent detection stability. These results suggest the potential of IGZO biosensors for specific and reliable detection of bladder-tumor-relevant proteins.

2.2. Clinical Investigations

To examine the applicability of IGZO FET biosensor for efficient bladder-tumor-relevant proteins detection in urine environment, an IGZO FET biosensor array consisting of five detection channels capable of parallel measurements of a group of bladder-tumor-relevant proteins, three control channels, and two Ag/AgCl reference electrodes were designed (**Figure 2**a). A set of clinical-relevant bladder tumor urine biomarkers was tested for detection and validation: NMP22, membrane antigen carbonic anhydrase 9 (CA9), cluster of differentiation 47 (CD47), cytokeratin 8 (CK8), and cytokeratin 18 (CK18). The rationale for target protein selection was based on previous studies of expression difference in BC at different stages.[1,8] To enable selective detection, five types of antibody molecules that are specific to these bladder-tumor-associated proteins were covalently functionalized on the IGZO FET biosensor array (Figure 2a; Figure S14, Supporting Information). The real-time and calibrated current responses of CA9, CD47, CK8, and CK18 antibody molecules functionalized IGZO biosensors toward CA9, CD47, CK8, and CK18 exhibit similar response performance as that of anti-NMP22/IGZO FET biosensor (Figures S15–S19, Supporting Information). The calculated detection limit (3 × standard deviation of the blank) of N-terminal functionalized IGZO biosensor array for NMP22, CA9, CD47, CK8, and CK18 is 3.2×10^{-17}, 6.2×10^{-18}, 3.7×10^{-17}, 1.6×10^{-18}, and 4.1×10^{-17} g mL^{-1}, which is ≈tenfold lower than that of C-terminal functionalized IGZO FET biosensors (7.3×10^{-16}, 2.5×10^{-16}, 8.1×10^{-16}, 6.8×10^{-16}, and 2.1×10^{-15} g mL^{-1} for NMP22, CA9, CD47, CK8 and CK18), 10^3 folds lower than that of electrochemical assay (10^{-14} g mL^{-1} level), 10^9 folds lower than that of fluorescence assays (10^{-8} g mL^{-1} level), and extremely lower than that of previously reported IGZO FET biosensors (Table S2, Supporting Information). The above results demonstrate that N-terminal functionalized IGZO biosensor array exhibits high sensitivity and could be used for rapid and facile identification of trace bladder-tumor-associated proteins.

With excellent detection performance, the IGZO FET biosensor array was incubated with freshly collected urine samples for subsequent analysis. NMP22, CA9, CD47, CK8, and CK18 protein signatures were collected. Figure 2b; Figure S20, Supporting Information, show that the IGZO FET biosensor array exhibits an obvious current variation upon exposing to BC patient urine samples, and the current response is significantly more obvious than that of healthy individuals. The intrinsic complexity of urine possibly would cause serious nonspecific adsorption and decrease the detection sensitivity and accuracy. Bovine serum albumin (BSA) was utilized to minimize non-specific adsorption and exclude weakly adsorbed biomolecules as validated by the increased current response after blocking (Figure 2c; Figure S21, Supporting Information). As conventional urinalysis approaches are not sufficiently sensitive to quantify the trace bladder-tumor-relevant proteins in urine samples, the recovery measurement was performed to evaluate the detection accuracy of IGZO FET biosensor array. By adding a series concentration of target proteins into urine samples, the recovery of spiked proteins was investigated and listed in Table S3, Supporting Information. The measured recovery ranges from 95.3% to 104.3%, indicating that our designed IGZO biosensor array is reliable for quantitative analysis of bladder-tumor-associated proteins in clinical patient urine samples. To explore the detection reproducibility of the

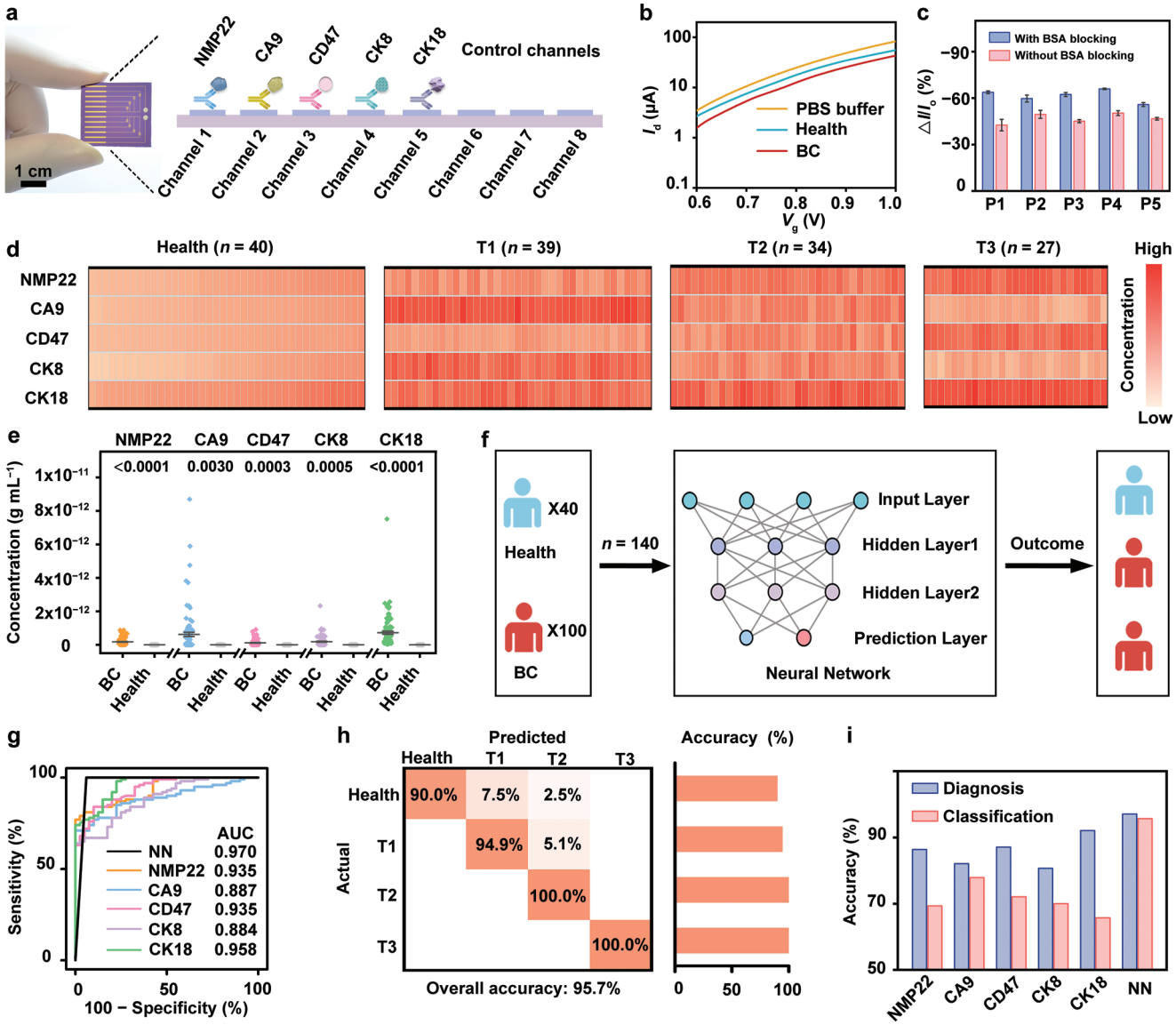

Figure 2. Clinical analysis of validation cohorts for BC diagnosis and classification. a) Photograph and schematic of eight-channel sensing array, in which five channels are functionalized with specific antibody molecules for bladder-tumor-relevant proteins, and the remaining three channels are utilized to record background signal of urine samples. b) I_d–V_g curves of anti-NMP22/IGZO FET biosensor array in response to the urine samples from a BC patient and a healthy individual. c) Current responses of anti-NMP22/FET biosensor array with and without BSA blocking for urine samples of five BC patients. P represents BC patients. No. 1–5 represents different patient samples. For example, "P1" represents a urine sample from BC patient No. 1. Error bars represent standard deviations of three measurements. d) Heat map of five bladder-tumor-relevant protein signatures in a training cohort. (n = 140; that is, 100 for untreated BC patients (including 39 cases in T1, 34 cases in T2, and 27 cases in T3) and 40 for healthy individuals. The color intensity indicates the concentration of protein. Among them, NMP22, CD47, and CK18 are up-regulated, CD47 and CK8 are down-regulated. e) Comparison of expression levels of five bladder-tumor-relevant proteins in urine samples from BC patients (n = 100) and healthy individuals (n = 40) ($P < 0.005$, unpaired two-sided t-test). f) Schematic diagram of NN algorithm for the identification and classification of BC. The NN algorithm comprises four layers: an input layer, two fully connected hidden layers, and a prediction layer. g) ROC curves showing high accuracy (AUC = 0.970) of NN algorithm in BC diagnosis, with its AUC significantly larger than that of a single protein. h) Confusion matrix summarizing the BC classification results in the training cohort. i) Discrimination of BC patients from healthy individuals and classification of BC stages based on NN algorithm or a single protein.

IGZO FET biosensor array, the current response of the biosensor toward the same BC patient urine sample was investigated. The response curves shown in Figure S22, Supporting Information, for the same patient urine sample are highly consistent (RSD below 7.7%), which shows excellent reproducibility for patient urine samples analysis. The excellent reproducibility of the biosensor array is mainly attributed to the large-area uniform IGZO channel materials and antibody immobilization layer. Based on the above results, it is expected that the IGZO biosensor array would be a powerful tool for identifying bladder-tumor-relevant proteins in human urine samples.

2.3. Clinical Validation Cohort

To enable clinical management diagnostics, following the prevalidation assays, we proceeded to patient-relevant testing with our IGZO FET biosensor array. We designed a training cohort with 100 patients (n = 100; 39 for stage I [T1], 34 for stage II [T2], and 27 for stage III [T3]) referred for clinically indicated BC diagnosed with image-guided aspiration and biopsy (Figure 2d; Table S4, Supporting Information). All the patients gave informed consent for the clinical validations. Urine samples of 40 healthy individuals were selected for comparison. The expression levels of NMP22, CA9, CD47, CK8, and CK18 in urine that were calculated based on the calibrated response curves in Figure 1e; Figure S23, Supporting Information were summarized in Figure 2d,e; Table S4, Supporting Information. Each patient shows particularly different protein expression levels (10^{-16} to 10^{-11} g mL^{-1} level), suggesting the diversity of bladder tumor phenotypes. The statistical expression levels of five bladder-tumor-associated proteins in BC patients are remarkably higher than in healthy individuals ($P < 0.005$), which is consistent with the upregulation expression theory of cancer.[44–46] Figure S23, Supporting Information also reveals upregulation of NMP22, CD47, CK18, and downregulation of CK8 and CA9 as the increase of BC stages, which are in good agreement with previously reported works.[47]

The difference in expression levels of bladder-tumor-associated proteins between BC patients and healthy individuals could potentially be used to give a discrimination. A machine-learning algorithm neural network (NN) was exploited to analyze and train the five protein signatures obtained by IGZO FET biosensor array to make a decision (Figure 2f). For the analysis of urine samples with a single protein signature, a cut-off value that could maximize the detection sensitivity and specificity was exploited. The predicted results were compared with cystoscopy and tumor biopsies to determine the accuracy of our biosensor platform. The receiver operating characteristic (ROC) curves and precision-recall curves derived from NN algorithm and a single protein signature were constructed (Figure 2g; Figure S24, Supporting Information). As indicated in Figure 2g, the area under the curve (AUC) of NN algorithm is significantly higher than those of individual protein signatures. The sensitivity and specificity for BC versus health differentiation predicted with NN algorithm reach 96.2% and 100%. In order to correlate antigen expression levels between BC stages and explore the capability of the biosensor for BC stages classification, the predicted and actual accuracy trained by NN algorithm with five protein signatures as inputs were mapped into a confusion matrix (Figure 2h). The NN algorithm generates a 94.9% accuracy for T1 BC identification, 100% accuracy for T2 BC identification, and 100% accuracy for T3 BC identification. The overall diagnosis accuracy and classification accuracy achieved with NN algorithm is 97.1% and 95.7% (95% confidence interval [CI]: 92.3–99.1%). Notably, these values are significantly higher than those calculated with single protein signatures (Figure 2I; Figure S25, Supporting Information). The above results validate that the simultaneous detection of five bladder-tumor-relevant proteins with IGZO FET biosensor array and the training of their combined protein signatures with NN algorithm are essential for effective BC diagnosis and classification.

2.4. Integrated Urinalysis Device for Point-of-Care Diagnosis

An ultimate goal of our platform is to enable efficient point-of-care or home-care diagnosis for decentralized remote healthcare. In this regard, we integrated the IGZO FET biosensor array with micro–nano fabrication and wireless technology to achieve a portable device for urine analysis (**Figure 3**a–c; Video S1, Supporting Information). The overall structure of the integrated urinalysis device mainly includes 1) an IGZO FET biosensor array for obtaining five bladder-tumor-associated protein signatures from untreated urine samples; 2) a device control panel for acquiring detection data from the biosensor array and information communicating; 3) a smartphone and an application program for data analysis and display (Figure 3b). The operation processes of the integrated urinalysis device are as follows: The microcontroller unit (MCU) in the data conversion module reads instructions from the smartphone via a wireless Bluetooth unit and transfers the instructions to voltage signal through a digital-to-analog converter (DAC). Then, the voltage following module magnifies the voltage signal and applies voltage toward IGZO FET biosensor array. Subsequently, the MCU sequentially accesses the measured current signal from IGZO FET biosensor array and converts the signal into readable information by an 8-to-1 multiplexer (MUX), a transimpedance amplifier (TIA), and an analog-to-digital converter (ADC). The Bluetooth unit exports the readable information to a smartphone, and the application program that incorporates NN algorithm and diagnosis interface could analyze the received information to display the diagnosis results (Figure 3d). The urinalysis device was compatible with a power source to supply the whole device. The integrated urinalysis device is a portable device with an overall dimension of 15.2 cm (L) × 6.5 cm (W) × 2.4 cm (H), and it could be directly used for data acquisition, information communication, and analysis (Figure 3c). Particularly, this stand-alone device could be easily operated by a variety of non-trained personnel and would not rely on well-instrumented laboratory or highly sophisticated analytical techniques. Specifically, after incubating 100 µL collected human urine directly on the device surface for 5 min, the integrated urinalysis device captures the bladder-tumor-associated protein signatures simultaneously and analyses the detection data with the assistance of application program incorporated with NN algorithm automatically to display the diagnosis results (Figure 3e,f; Videos S2 and S3, Supporting Information). Owing to the fast response speed of IGZO FET biosensor and the efficient detection signal transmission, the whole urinalysis process only requires less than 10 min. The diagnosis results displayed in Figure 3e,f validate that the integrated urinalysis device could achieve efficient BC identification and classification. Notably, the component of urine is particularly complex and is influenced by human activities such as diet, rest, and movements, while the integrated urinalysis device with high stability and uniform biosensor array presents the ability to achieve parallel measurements of five protein signatures from urine samples. These features promise the potential of the integrated urinalysis device for clinical utility, point-of-care settings, and health clinics in rural areas.

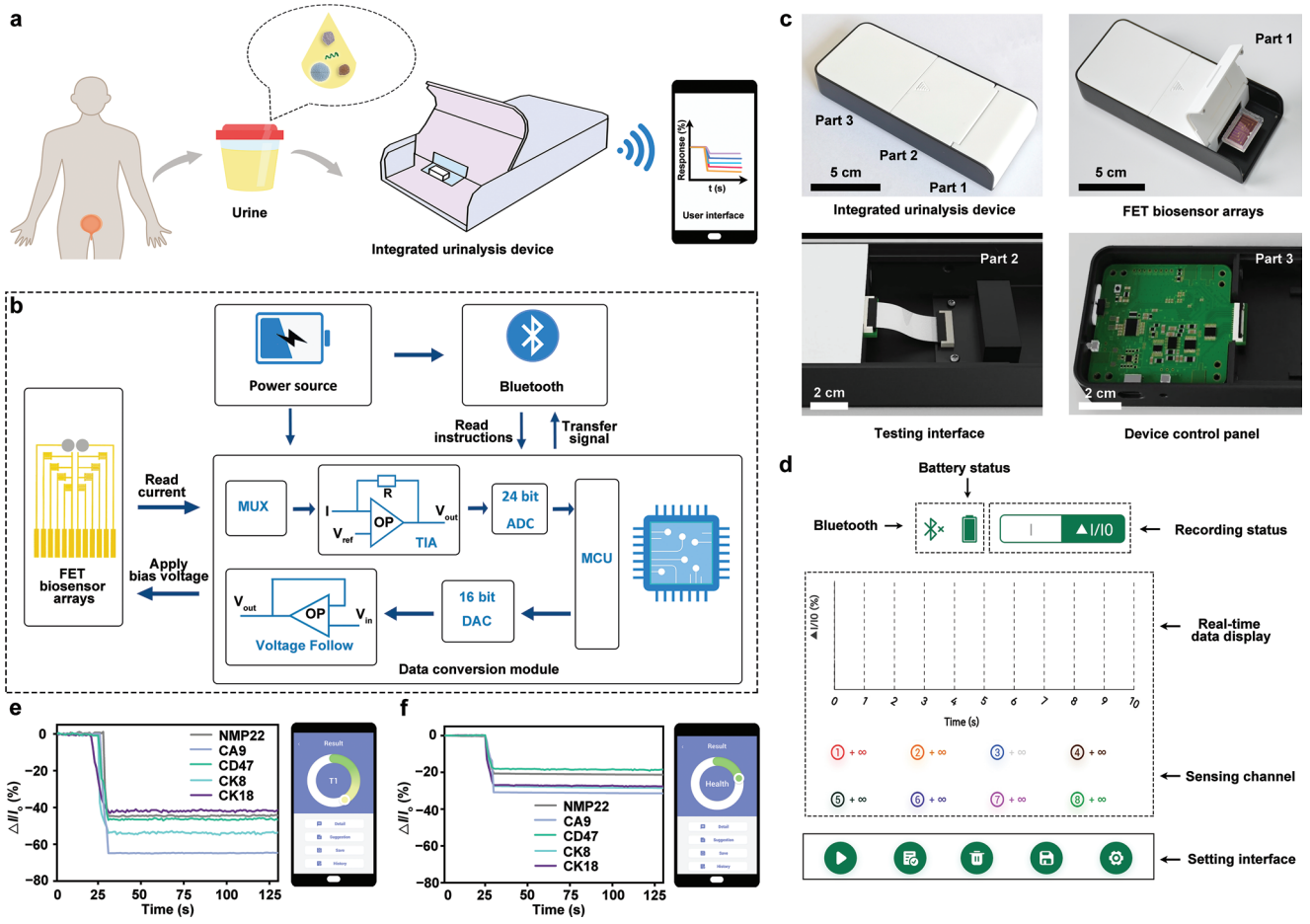

Figure 3. Integrated urinalysis device for point-of-care diagnosis. a) Schematic of integrated urinalysis device for the detection of urine samples. b) Circuit diagram and working principle of the integrated urinalysis device. c) Photograph of the integrated urinalysis device and the enlargement images of the three parts. d) Testing interface and operation interface on the smartphone. e,f) Current responses and diagnosis results of the integrated urinalysis device toward a BC patient (e) and a healthy individual (f).

2.5. Double-Blind Prediction

To explore the clinical utility of the integrated urinalysis device, a testing cohort of patients (n = 65) with unknown diagnosis information and non-BC individuals (10 healthy individuals and 25 non-BC patients with urinary diseases) was selected for a blind prediction (**Figure 4**a and **Table 1**). The expression levels of bladder-tumor-associated proteins summarized in Figure 4b; Figure S26, Supporting Information indicate that the BC patients show significantly high protein expression levels than non-BC patients and healthy individuals ($P < 0.005$). The prediction performance was evaluated with cystoscopy and tumor biopsies diagnosis results. As shown in Figure 4c,d and Table 1, a sensitivity of 100.0% and a specificity of 92.1% were achieved based on the ROC and precision-recall curves, and these values are significantly higher than that estimated by urine cytology (sensitivity of 48.0% and specificity of 86.0%) and fluorescence in situ hybridization (FISH, 62.0% in sensitivity and 90.0% in specificity).[47–49] These prediction results indicate that the integrated urinalysis device could enable effective BC diagnosis. For a further step, we explored the capability of the integrated urinalysis device for BC stages classification with the same testing cohort. As indicated in Figure 4e, the integrated urinalysis device could identify T1 BC with an accuracy of 84.2%, T2 BC with an accuracy of 87.5%, and T3 BC with an accuracy of 66.7%. The overall accuracy for BC diagnosis and classification with our established NN algorithm remains 95.0% and 90.0% (95% CI: 84.1–95.9%), significantly higher than those calculated with single protein signatures (Figure S27, Supporting Information). To further investigate the cancer stages classification capability of our integrated urinalysis device, we performed clinically applicable H&E histological analysis for selected BC patients. It is recognized that with the development of BC, the tumor cells would gradually invade the bladder wall and even surrounding tissues, and the nuclei of tumor cells would grow larger and irregular.[50] Based on these considerations, the BC stages were classified as shown in the H&E images in Figure 4f; Figures S28–S30, and the classification results display good concordance with those obtained by urinalysis. The above analysis suggests that the integrated urinalysis device could be utilized in BC stages classification effectively. The reliable protein signatures identification capability and the high accuracy in BC diagnosis and classification possibly benefit from the high sensitivity, stability biosensor arrays,

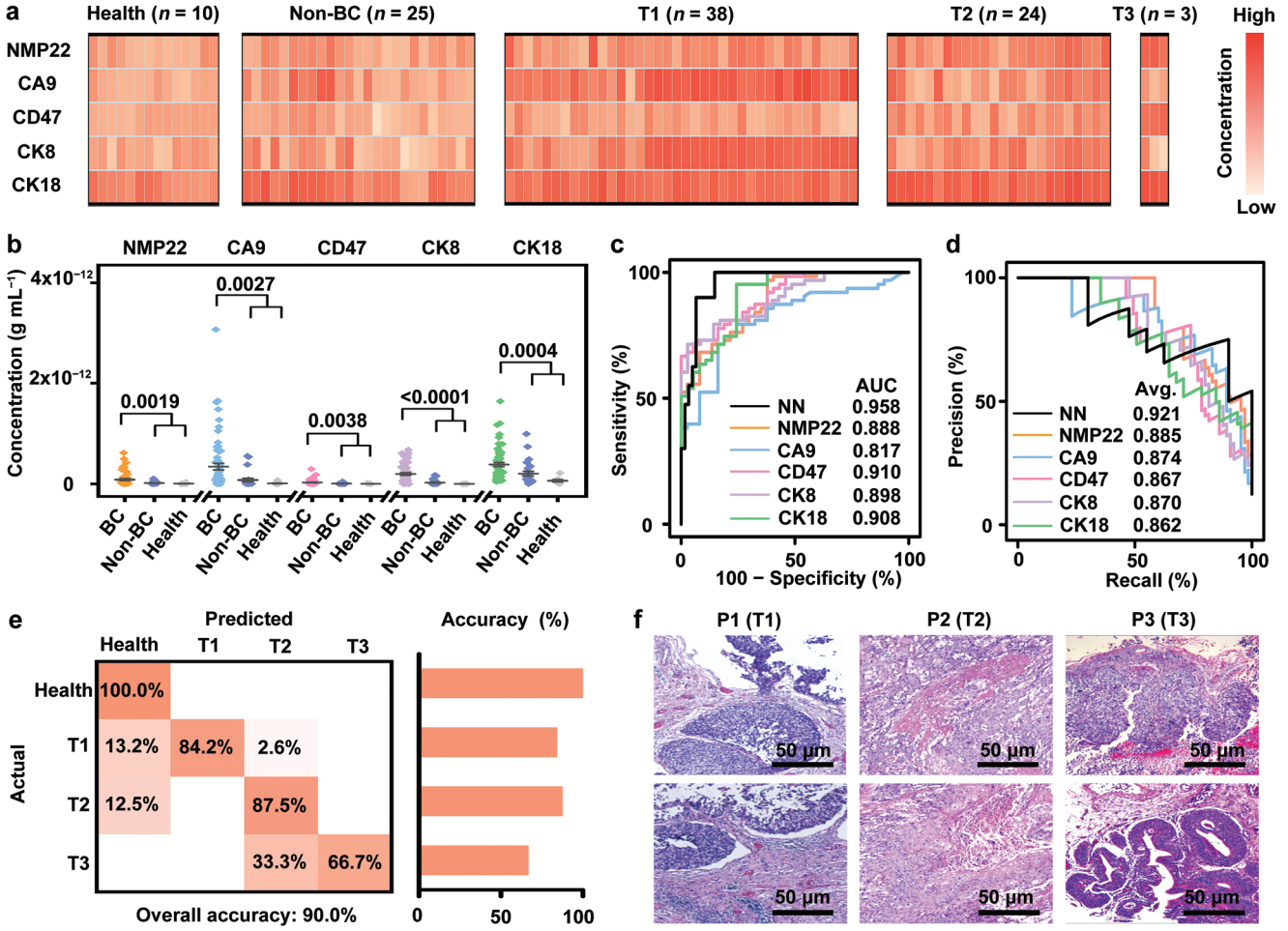

Figure 4. Blind prediction of testing cohorts for BC diagnosis and classification. a) Application of the trained NN algorithm for the analysis of an independent testing cohort ($n = 100$; that is, 38 for T1, 24 for T2, 3 for T3, 25 for non-BC, and 10 for healthy individuals). The concentrations of five proteins were shown by heat map. b) Protein expression levels in urine samples from BC patients, non-BC patients, and healthy individuals ($P < 0.005$, unpaired two-sided t-test). c,d) ROC and precision-recall curves for the prediction of sensitivity and specificity in BC diagnosis based on NN algorithm and a single protein signature. The AUC of the NN algorithm is significantly higher than that of a single protein. e) Confusion matrix summarizing the BC classification results in a testing cohort. f) Six representative tumor tissue images showing three BC patients at different stages.

Table 1. Summary of BC diagnostic statistics for single proteins and protein combination.

Markers		Training cohort ($n = 140$)						Testing cohort ($n = 100$)			
		AUC	Avg. precision	Sensitivity [%]	Specificity [%]	Diagnosis accuracy [%]	Classification [%]	Sensitivity [%]	Specificity [%]	Diagnosis accuracy [%]	Classification [%]
Single proteins	NMP22	0.935	0.935	92.0	85.2	86.4	69.3	79.3	83.1	82.0	68.0
–	CA9	0.887	0.922	69.2	87.1	82.1	77.9	83.3	85.7	85.0	63.0
–	CD47	0.935	0.934	87.1	89.3	87.1	72.1	78.4	91.7	87.0	67.0
–	CK8	0.884	0.918	84.1	67.9	80.7	70.0	81.8	79.5	79.0	65.0
–	CK18	0.958	0.941	91.6	93.9	92.1	65.7	85.1	92.3	89.0	67.0
Protein combination	NN	0.970	0.968	96.2	100.0	97.1	95.7	100.0	92.1	95.0	90.0
Clinical methods	Urinary cytology	–	–	–	–	–	–	48.0	86.0	–	–
–	FISH	–	–	–	–	–	–	62.0	90.0	–	–

and systematic database treatment with NN algorithm. These results highlight the ability of the integrated urinalysis device in identifying BC status, opening up the possibility to track the progression of BC.

2.6. Longitudinal Monitoring During Clinical Care

Longitudinal monitoring of protein signatures of BC patients could provide critical information regarding the progression of BC and enable effective prognosis. Especially, recording the real-time protein signatures offers the possibility to evaluate the cancer risk and provide the corresponding treatment strategy. Consequently, serial protein signatures of a cohort of patients (n = 16 for T1 patients and n = 16 for T2 patients) before and after surgery were tracked with the integrated urinalysis device (**Figure 5**a, Figure S31, Supporting Information). Urine samples were collected 24 h before surgery and within one week after surgery. As shown in Figure 5a, the concentrations of proteins show an obvious decrease in all the patients, presumably due to the decreased proteins expression level in urine after curative tumor resection. To clearly present the change of protein signatures, the longitudinal protein signatures of NMP22, CA9, CD47, CK8, and CK18 were summarized in Figure 5b–f for T1 BC patients (n = 16) and in Figure 5g–k for T2 BC patients (n = 16). It can be clearly observed that all the investigated proteins show an obvious decrease, and this tendency is particularly notable for T2 patients (P < 0.05, paired t-test). Serial monitoring of bladder-tumor-relevant protein signatures thus proposes a general strategy for cancer recurrence evaluation and prognosis tracking.

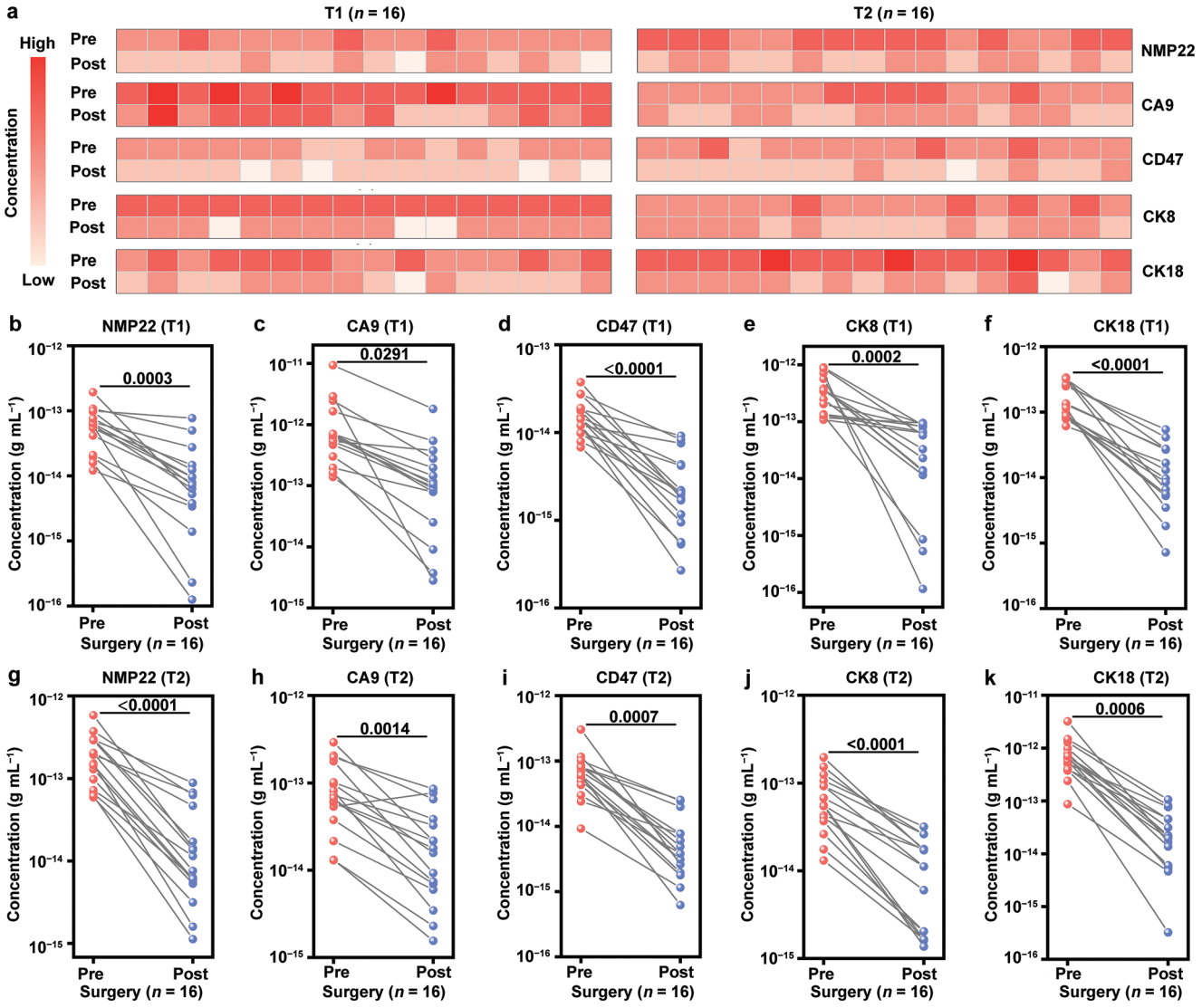

Figure 5. Longitudinal monitoring during clinical care. a) Urine samples from BC patients (n = 32; 16 for T1 and 16 for T2) before and after surgery were analyzed by the integrated urinalysis device. The expression levels of five protein signatures were summarized by heat map. b–k) Changes in the expression levels of five bladder-tumor-relevant protein signatures from T1 and T2 BC patients before and after surgery (P < 0.05, paired two-sided t-test). (b) and (g) represent the changes of NMP22 level in urine samples from T1 and T2 BC patients before and after surgery, respectively. (c,h), (d,i), (e,j), and (f,k) represent CA9, CD47, CK8, and CK18, respectively.

3. Conclusion

This work presents an integrated urinalysis device that is composed of an IGZO FET biosensor array, a device control panel, and an Internet terminal to identify and analyze a group of bladder-tumor-relevant proteins in urine samples for the achievement of clinical management. The interface of IGZO FET biosensor with excellent electrical performance was engineered to decrease the Debye screening effect originating from the high ionic strength of urine, thus enabling its capability for direct analysis of protein signatures in freshly collected urine samples. The urinalysis revealed that the bladder-tumor-associated proteins in urine could reflect the critical signature of BC, and the simultaneous detection and analysis of a panel of protein is necessary for efficient BC identification and cancer stages classification due to the intrinsic heterogeneous nature of tumor. Through the training of five protein signatures in urine samples from a cohort of 197 BC patients and 75 non-BC individuals, the integrated urinalysis device could achieve a 95.0% diagnosis accuracy and a 90.0% cancer stages classification accuracy. In addition, the protein signatures show a significant correlation with treatment response. The serial monitoring of protein signature reflects that the protein expression levels decreased in all BC patients after surgical treatment, demonstrating the potential of the integrated urinalysis device for BC treatment monitoring, risk evaluation, and prognosis. The integrated urinalysis device with the characteristics of portability, low-cost, non-invasiveness, and automated data treatment and analysis that can be operated by non-trained personnel could potentially translate into standard clinical practice for cancer or critical diseases diagnostics and prognosis. A similar platform can be adapted for analysis of the other body fluids including blood and saliva for the point-of-care diagnosis of a wide range of biomarkers for personalized medicine.

4. Experimental Section

Materials and Reagents: Methanol, ethanol, isopropyl alcohol, acetone, glutaraldehyde (25.0%), polyvinyl butyral (PVB), and iron(III) chloride ($FeCl_3$, >99.0%) were purchased from Sinopharm Chemical Reagent Co., Ltd. EDC, NHS, poly(methyl methacrylate) (PMMA), and APTES were obtained from Aladdin. BSA and PBS (0.1×10^{-3} M, 1×10^{-3} M, and 10×10^{-3} M, pH 7.4) were bought from Shanghai Yuanye Bio-Technology Co., Ltd. Bladder-tumor-relevant proteins NMP22, CA9, CD47, CK8, CK18 and the corresponding antibody molecules anti-NMP22, anti-CA9, anti-CD47, ani-CK8, and anti-CK18 were purchased from Dafeng Biotechnology Co., Ltd. The detailed information of these proteins is listed in Table S5, Supporting Information.

Instrument and Characterization: The metallic electrodes (Cr/Au) array was patterned by ultraviolet (UV) lithography (ABM. Inc, America) and deposited by a thermal evaporator system (Jiashuo JSD-300, China). The IGZO channel layer was deposited by a radio frequency sputtering system with the assistance of mask templates (Jiashuo JSD300-II, China). The sensing area of the FET biosensor was exposed by an electron beam lithography system (EBL, JSM-6510, Japan). The microscopy images of the IGZO sensing electrodes were obtained with an optical microscope (Olympus BX53MRF-S). The immobilization of antibody molecules on the IGZO surface was characterized by XPS (ESCAI AB250Xi, USA) and ATR-FTIR (FTIR5700, USA). The surface morphology and thickness of IGZO layer were characterized by AFM (Park nx10, Korea), ellipsometer (J.A. Woollam M-2000, USA), and high-resolution field emission SEM (FEI Verios 460, USA). The ellipsometer characterization was performed at wavelength between 300 and 1000 nm at the incident angles of 65°, 70°, and 75°. The functionalized thickness of anti-NMP22 on the device was fitted by the Cauchy model. The electrical characteristics of the IGZO FET device were measured by a digital source meter (Agilent B2902A, USA) connected to a probe station.

Clinical Samples: Urine samples of BC patients were provided by the Union Hospital of Wuhan and Renmin Hospital of Wuhan University. Urine samples of healthy individuals and non-BC patients were collected from Wuhan University and Renmin Hospital of Wuhan University. All relevant ethical laws and regulations concerning human participants were complied with. The study was approved by the Ethics Committee of Union Hospital of Wuhan and Renmin Hospital of Wuhan University. All the participants in this study signed informed consent forms before participating. In this study, the gender, age and pathological diagnosis results of all clinical samples were recorded anonymously.

H&E Histological Analysis: Histological analysis of bladder tumor tissues was performed by paraffin-embedded tissue sections fixed with 10% formalin. The bladder tumor tissue samples were sectioned at a thickness of 5 μm and stained with hematoxylin and eosin (H&E) for imaging. The images were obtained with an Olympus CKX53 inverted microscope slide scanner at 100× magnification.

Fabrication of IGZO FET Array: The IGZO FET array was fabricated by the following processes. First, the interdigital source, drain, and gate electrodes (15 nm Cr/50 nm Au) were deposited with thermal evaporation after patterning by photolithography. The channel length and width were 480 and 500 μm, respectively. Then, the IGZO channel layer was deposited between patterned source and drain electrodes by magnetron sputtering with the assistance of a mask template. Ag/AgCl reference electrodes were fabricated by sequentially dip-coating silver colloid on the gate electrode, heating at 75 °C for 15 min to evaporate solvent, dropping 0.1 M $FeCl_3$ solution on the silver colloid and reacting for 4 min to form AgCl layer. The surface of AgCl electrode was then treated with PVB-methanol solution for 3 h at room temperature to form a protective layer.

IGZO FET Electrical Characteristics Evaluation: The μ_{FE} and transconductance (g_m) of IGZO device were calculated based on the transfer characteristic curves in Figure S2, Supporting Information. As the interdigital electrode is composed of four independent electrodes in parallel, the μ_{FE} of IGZO device is 1/4 of the apparent and it can be calculated by:

$$\mu_{FE} = \frac{g_m L}{4WV_d C_{ox}} = \frac{dI_d L}{dV_g 4WV_d C_{ox}} \quad (2)$$

where L and W represent the channel length (480 μm) and width (500 μm). C_{ox} is 11.5 nF cm^{-2} for Si wafer with 300 nm SiO_2 dielectric layer. V_d is set at 0.2 V. Based on Equation (2), it is calculated that the μ_{FE} of IGZO device is 15. 8 cm^2 V^{-1} s^{-1}. The obtained maximized value of g_m calculated by I_d–V_g curve is 1.0 μS.

Fabrication of IGZO FET Biosensor Array: To achieve selective functionalization of antibody molecules on the IGZO sensing channel and avoid gate leakage current, the IGZO FET array was spin-coated with a layer of PMMA as protection layer and the IGZO sensing region with an area of 480 × 500 μm^2 was exposed by electron beam lithography. The device was then integrated with a PDMS well (with 2.5 cm length, 1.5 cm width, and 0.3 cm height) for selective functionalization and sensing. Subsequently, the IGZO layer was covalently functionalized with APTES to introduce amine groups on the IGZO. Specifically, 1 mL of 5% APTES in ethanol was dropped into the PDMS chamber for 1 h and then heated in an oven at 110 °C for 30 min to strengthen the silanization of APTES.[51] Then, 1 mL glutaraldehyde (5%) PBS buffer solution was added into the chamber and reacted for 2 h at room temperature to serve as linker molecules for conjugating N-terminal antibody molecules. To obtain N-terminal functionalized IGZO FET biosensor, 100 μL antibody solution was added onto the IGZO channel and coupled with glutaraldehyde for 12 h at 4 °C.[52] After BSA (0.01 g mL^{-1}) blocking at 4 °C for 12 h and PBS buffer washing, N-terminal functionalized IGZO FET biosensor was obtained. C-terminal functionalized IGZO FET biosensor was prepared by sequentially adding

4 mL of EDC/NHS PBS solution (containing 20 µg EDC and 10 µg NHS) and 100 µL antibody solution onto the surface of APTES functionalized IGZO FET array, and shaking at room temperature for 2 h to couple with C-terminal antibody. It is worth noting that the 8-channel sensing array consists of five detection channels for parallel measurements and three control channels for background signal recording. The control channels were obtained by blocking glutaraldehyde coupled IGZO with BSA to minimize urine environment such as ion strength and pH on the influence of sensing performance. To explore the optimized antibody functionalization concentration, a series of antibody solutions with concentrations ranging from 10–30 µg mL^{-1} was investigated (Figure S8, Supporting Information). Based on the measured current response, it is determined that the optimized concentration for anti-NMP22, anti-CA9, anti-CD47, anti-CK8, and anti-CK18 is 20 µg mL^{-1}.

Detection of Bladder-Tumor-Relevant Proteins: Before the measurements, the target protein incubation time was determined as 5 min to achieve the optimized current response (Figure S9, Supporting Information). To investigate the relationship between ionic strength of PBS buffer and current response of biosensor, the current response of anti-NMP22/IGZO FET biosensor toward NMP22 target (10^{-16} g mL^{-1}) was recorded under different concentrations of PBS buffer (0.1–10 × 10^{-3} M). The real-time current response (I_d–t curves) of molecular specificity IGZO FET biosensor array was measured by successively injecting 100 µL target protein solution with a range of concentrations (10^{-16} to 10^{-6} g mL^{-1}) into the PDMS chamber. The calibrated response curves were recorded by measuring the current response of the IGZO FET biosensor array before and after target proteins conjugation. The I_d–V_g curves were recorded at V_d = 0.2 V. The I_d–t curves were recorded at V_d = 0.2 V and V_g = 0.6 V. The selectivity of the IGZO FET biosensor array was evaluated by monitoring each antibody molecule functionalized IGZO FET biosensor unit toward the target protein and interfering molecules. For example, for NMP22 specific IGZO FET biosensor, NMP22 was used as the target, and CA9, CD47, CK8, and CK18 were selected as interfering molecules. The concentrations of the target and interfering molecules were all 10^{-12} g mL^{-1}. The recovery measurements were performed by adding a series concentration of target proteins into the urine samples and calculating the found target proteins concentration.

Construction of Integrated Urinalysis Device: The portable urinalysis device was integrated by an IGZO FET biosensor array, a Li-ion battery, a Bluetooth unit, a multiplexer (MUX), a trans-impedance amplifier (TIA), an analogue-to-digital converter (ADC), a digital-to-analogue converter (DAC), a voltage following module, and a microcontroller (MCU) unit. The NN algorithm was input into the smartphone to realize the analysis of the received data. An application program that includes operation interfaces, testing interfaces, and diagnosis results interfaces for real-time data presentation and analysis, was also developed. The diagnosis results could be presented on the interface to provide clinical suggestions and the corresponding diagnosis data could be saved in the smartphone.

Clinical Urine Samples Analysis: For clinical urine samples real-time detection, the integrated urinalysis device was first exposed to PBS electrolyte to record the initial current value I_o and then the specific current signal was recorded after adding 100 µL urine samples into the PBS electrolyte. The urine incubation time remained for 5 min. The average current signal was generated by recording the current responses of the device toward a specific urine sample for 60 s. A training cohort of 100 BC patients and 40 healthy individuals as well as a testing cohort of 65 BC patients, 25 non-BC patients, and 10 healthy individuals was used for evaluation. The protein concentration was calculated based on the linear range in the calibrated response curves in Figure 1e; Figure S16, Supporting Information. The obtained protein signatures were used for subsequent machine-learning analysis.

Machine Learning for BC Diagnosis and Classification: NN model for BC diagnosis and classification was used in this study. Specifically, each biomarker value was set as an input feature x_i. Let a feature vector $x = [x_1, x_2, \cdots, x_n]$ denote n biomarker values. To deal with the numerical instability problem that the original marker values are too low (<10^{-9}), features were standardized by removing the mean and scaling to unit variance,

$$x' = \frac{x - \mu}{\sigma} \tag{3}$$

where μ denotes the mean of the training sample and σ is the standard deviation of the training samples.

Then, multilayer perceptron (MLP) was used to learn a classifier for cancer classification,

$$x_{h+1} = \varphi(x_h \cdot W + b) \tag{4}$$

where x_h is the input vector for h–th linear layer, W is the weight, and b is the bias. In this work's experiments, the dimension of hidden layers is optimized and fixed as 100. The layer number is 3. φ is the ReLU activation function.

In the last layer, a softmax classifier was used to predict,

$$c = \arg\max_i \frac{\exp(\dot{x})}{\sum_K \exp(\dot{x}_i)} \lim_{x \to \infty} \tag{5}$$

where $\dot{x}$ denotes the output vector of the last layer. $K = 4$ is the number of types, including {Health, T_1,T_2,T_3}. c is the predicting class. The hyperparameters of the neural network were optimized by the adaptive stochastic gradient descent method.[53]

The detailed analysis processes are as follows. The whole samples collected in this paper were randomly split into the training set (60%) and the blind testing set (40%). The diagnostic efficiency of the algorithm was evaluated based on the concentrations of five protein signatures fed into the output of the NN algorithm. The AUC values of ROC curves, accuracy, recall, and precision were reported for evaluating this work's models. These models were implemented with an open-source machine-learning toolkit, Scikit-Learn, in the platform of Python 3.8.1, Ubuntu Linux 16.04 LTS.[54] The hardware environment was with Intel Xeon CPU E5-2620, NVIDIA TITAN Xp*3. In order to deploy this classification model in portable mobile devices, the weights trained by this model were exported and the model was refactored with C++ environment.

Statistical Analysis: The sensing current response of clinical samples was obtained from five parallel tests and expression levels of bladder-tumor-relevant proteins were organized in the heat maps via Origin 2022 (https://www.originlab.com/). The significance between expression levels of five bladder-tumor-relevant proteins in urine samples from BC patients and healthy individuals was tested using an unpaired two-sided t-test. The significance between expression levels of five bladder-tumor-relevant protein signatures before and after surgery was tested using a paired two-sided t-test. Statistical significance of the data was calculated at 95% ($P < 0.05$) CIs. ROC and precision-recall curves were constructed to evaluate the accuracy of bladder cancer diagnosis and classification. Sensitivity was defined as the probability that a test result was positive when cancer was detected (true positive rate), specificity as the probability that a test result was negative when cancer was not detected (true negative rate), and accuracy as the overall probability that an individual was correctly classified. The 95% CIs were calculated using a binomial distribution. Significance analyses, construction of ROC and precision-recall curves, and AUC calculation were performed using GraphPad Prism 8 (https://www.graphpad.com/scientific-software/prism/).

Supporting Information

Supporting Information is available from the Wiley Online Library or from the author.

Acknowledgements

Y.Y. and J.W. contributed equally to this work. This work was supported by funding from the National Key R&D Program of China (2017YFA0208000,

2021YFA1202400), the National Natural Science Foundation of China (21925401, 21904033), and the Fundamental Research Funds for the Central Universities (2042021kf0036, 2042022kf0028). The authors thank the Core Facility of Wuhan University for large-scale instrument and equipment sharing foundation.

Conflict of Interest

The authors declare no conflict of interest.

Data Availability Statement

The data that support the findings of this study are available from the corresponding author upon reasonable request.

Keywords

bladder cancer, healthcare monitoring devices, machine learning, transistor biosensors, urinalysis

Received: April 10, 2022
Revised: July 12, 2022
Published online: August 7, 2022

[1] A. M. Kamat, N. M. Hahn, J. A. Efstathiou, S. P. Lerner, P.-U. Malmström, W. Choi, C. C. Guo, Y. Lotan, W. Kassouf, *Lancet* **2020**, *388*, 2796.
[2] S. Antoni, J. Ferlay, I. Soerjomataram, A. Znaor, A. Jemal, F. Bray, *Eur. Urol.* **2017**, *71*, 96.
[3] A. G. Robertson, J. Kim, H. Al-Ahmadie, J. Bellmunt, G. Guo, A. D. Cherniack, T. Hinoue, P. W. Laird, K. A. Hoadley, R. Akbani, M. A. A. Castro, E. A. Gibb, R. S. Kanchi, D. A. Gordenin, S. A. Shukla, F. Sanchez-Vega, D. E. Hansel, B. A. Czerniak, V. E. Reuter, X. Su, B. de Sa Carvalho, V. S. Chagas, K. L. Mungall, S. Sadeghi, C. S. Pedamallu, Y. Lu, L. J. Klimczak, J. Zhang, C. Choo, A. I. Ojesina, et al., *Cell* **2017**, *171*, 540.
[4] X. Wei, F. Bian, X. Cai, Y. Wang, L. Cai, J. Yang, Y. Zhu, Y. Zhao, *Anal. Chem.* **2020**, *92*, 6121.
[5] E. J. Kouba, L. Cheng, *JAMA Oncol.* **2017**, *3*, 1570.
[6] C. Pettenati, M. A. Ingersoll, *Nat. Rev. Urol.* **2018**, *15*, 615.
[7] T. Powles, J. P. Eder, G. D. Fine, F. S. Braiteh, Y. Loriot, C. Cruz, J. Bellmunt, H. A. Burris, D. P. Petrylak, S.-l. Teng, X. Shen, Z. Boyd, P. S. Hegde, D. S. Chen, N. J. Vogelzang, *Nature* **2014**, *515*, 558.
[8] A. M. Kamat, P. K. Hegarty, J. R. Gee, P. E. Clark, R. S. Svatek, N. Hegarty, S. F. Shariat, E. Xylinas, B. J. Schmitz-Drager, Y. Lotan, L. C. Jenkins, M. Droller, B. W. van Rhijn, P. I. Karakiewicz, *Eur. Urol.* **2013**, *63*, 4.
[9] H. M. Huang, H. X. Li, *Cancer Commun.* **2021**, *41*, 91.
[10] F. Descotes, N. Kara, M. Decaussin-Petrucci, E. Piaton, F. Geiguer, C. Rodrigurz-Lafrasse, J. E. Terrier, J. Lopez, A. Ruffion, *Br. J. Cancer* **2017**, *117*, 583.
[11] C. Liu, J. Zhao, F. Tian, L. Cai, W. Zhang, Q. Feng, J. Chang, F. Wan, Y. Yang, B. Dai, Y. Cong, B. Ding, J. Sun, W. Tan, *Nat. Biomed. Eng.* **2019**, *3*, 183.
[12] J. Deng, F. Tian, C. Liu, Y. Liu, S. Zhao, T. Fu, J. Sun, W. Tan, *J. Am. Chem. Soc.* **2021**, *143*, 7261.
[13] J. Zhou, Z. Wu, J. Hu, D. Yang, X. Chen, Q. Wang, J. Liu, M. Dou, W. Peng, Y. Wu, W. Wang, C. Xie, M. Wang, Y. Song, H. Zeng, C. Bai, *Sci. Adv.* **2020**, *6*, eabc1204.
[14] G. Siravegna, S. Marsoni, S. Siena, A. Bardelli, *Nat. Rev. Clin. Oncol.* **2017**, *14*, 531.
[15] C. L. Ji, J. Tan, Q. Yuan, *Chin. J. Chem.* **2021**, *39*, 3188.
[16] Y. M. D. Lo, D. S. C. Han, P. Jiang, R. W. K. Chiu, *Science* **2021**, *372*, eaaw3616.
[17] Q. Zhou, J. Pan, S. Deng, F. Xia, T. Kim, *Adv. Mater.* **2021**, *33*, 2008276.
[18] M. Ratner, *Nat. Biotechnol.* **2018**, *36*, 209.
[19] L. Cai, S. Zhang, J. Miao, Z. Yu, C. Wang, *ACS Nano* **2016**, *10*, 11459.
[20] A. Clifford, J. Das, H. Yousefi, A. Mahmud, J. B. Chen, S. O. Kelley, *J. Am. Chem. Soc.* **2021**, *143*, 5281.
[21] A. R. J. Lawson, F. Abascal, T. H. H. Coorens, Y. Hooks, L. O'Neill, C. Latimer, K. Raine, M. A. Sanders, A. Y. Warren, K. T. A. Mahbubani, B. Bareham, T. M. Butler, L. M. R. Harvey, A. Cagan, A. Menzies, L. Moore, A. J. Colquhoun, W. Turner, B. Thomas, V. Gnanapragasam, N. Williams, D. M. Rassl, H. Vöhringer, S. Zumalave, J. Nangalia, J. M. C. Tubío, M. Gerstung, K. Saeb-Parsy, M. R. Stratton, P. J. Campbell, et al., *Science* **2020**, *370*, 75.
[22] J. Kaiser, *Science* **2018**, *359*, 259.
[23] Z. Ou, K. Li, T. Yang, Y. Dai, M. Chandra, J. Ning, Y. Wang, R. Xu, T. Gao, Y. Xie, Q. He, Y. Li, Q. Lu, L. Wang, Z. Song, *Clin. Transl. Med.* **2020**, *9*, 4.
[24] S. M. Park, D. D. Won, B. J. Lee, D. Escobedo, A. Esteva, A. Aalipour, T. J. Ge, J. H. Kim, S. Suh, E. H. Choi, A. X. Lozano, C. Yao, S. Bodapati, F. B. Achterberg, J. Kim, H. Park, Y. Choi, W. J. Kim, J. H. Yu, A. M. Bhatt, J. K. Lee, R. Spitler, S. X. Wang, S. S. Gambhir, *Nat. Biomed. Eng.* **2020**, *4*, 624.
[25] Y. Yu, H. Jin, D. Holder, J. S. Ozer, S. Villarreal, P. Shughrue, S. Shi, D. J. Figueroa, H. Clouse, M. Su, N. Muniappa, S. P. Troth, W. Bailey, J. Seng, A. G. Aslamkhan, D. Thudium, F. D. Sistare, D. L. Gerhold, *Nat. Biotechnol.* **2010**, *28*, 470.
[26] Y. Q. Liang, M. M. Xiao, D. Wu, Y. X. Lin, L. J. Liu, J. P. He, G. J. Zhang, L. M. Peng, Z. Y. Zhang, *ACS Nano* **2020**, *14*, 8866.
[27] J. X. Liu, X. H. Chen, Q. Q. Wang, M. M. Xiao, D. L. Zhong, W. Sun, G. Y. Zhang, Z. Y. Zhang, *Nano Lett.* **2019**, *19*, 1437.
[28] Y. Yang, X. Yang, X. Zou, S. Wu, D. Wan, A. Cao, L. Liao, Q. Yuan, X. Duan, *Adv. Funct. Mater.* **2017**, *27*, 1604096.
[29] Y. Liu, X. Duan, H. J. Shin, S. Park, Y. Huang, X. Duan, *Nature* **2021**, *591*, 43.
[30] J. Y. Oh, S. Rondeau-Gagne, Y. C. Chiu, A. Chortos, F. Lissel, G. N. Wang, B. C. Schroeder, T. Kurosawa, J. Lopez, T. Katsumata, J. Xu, C. Zhu, X. Gu, W. G. Bae, Y. Kim, L. Jin, J. W. Chung, J. B. Tok, Z. Bao, *Nature* **2016**, *539*, 411.
[31] V. K. Sangwan, H. S. Lee, H. Bergeron, I. Balla, M. E. Beck, K. S. Chen, M. C. Hersam, *Nature* **2018**, *554*, 500.
[32] H. Lee, S. Lee, Y. Kim, A. B. Siddik, M. M. Billah, J. Lee, J. Jang, *IEEE Electron Device Lett.* **2020**, *41*, 1520.
[33] B. Jiang, Z. Yang, X. Liu, Y. Liu, L. Liao, *Nano Today* **2019**, *25*, 122.
[34] Y. Wang, J. C. Kim, R. J. Wu, J. Martinez, X. Song, J. Yang, F. Zhao, A. Mkhoyan, H. Y. Jeong, M. Chhowalla, *Nature* **2019**, *568*, 70.
[35] P. Lin, F. Yan, *Adv. Mater.* **2012**, *24*, 34.
[36] C. Qiu, Z. Zhang, M. Xiao, Y. Yang, D. Zhong, L.-M. Peng, *Science* **2017**, *355*, 271.
[37] R. Hajian, S. Balderston, T. Tran, T. deBoer, J. Etienne, M. Sandhu, N. A. Wauford, J. Y. Chung, J. Nokes, M. Athaiya, J. Paredes, R. Peytavi, B. Goldsmith, N. Murthy, I. M. Conboy, K. Aran, *Nat. Biomed. Eng.* **2019**, *3*, 427.
[38] M. Ku, J. Kim, J.-E. Won, W. Kang, Y.-G. Park, J. Park, J.-H. Lee, J. Cheon, H. H. Lee, J.-U. Park, *Sci. Adv.* **2020**, *6*, eabb2891.
[39] C. Dai, M. Guo, Y. Wu, B. P. Cao, X. Wang, Y. Wu, H. Kang, D. Kong, Z. Zhu, T. Ying, Y. Liu, D. Wei, *J. Am. Chem. Soc.* **2021**, *143*, 19794.
[40] C. Sun, R. Li, Y. Song, X. Jiang, C. Zhang, S. Cheng, W. Hu, *Anal. Chem.* **2021**, *93*, 6188.

[41] D. Kong, X. Wang, C. Gu, M. Guo, Y. Wang, Z. Ai, S. Zhang, Y. Chen, W. Liu, Y. Wu, C. Dai, Q. Guo, D. Qu, Z. Zhu, Y. Xie, Y. Liu, D. Wei, *J. Am. Chem. Soc.* **2021**, *143*, 17004.
[42] A. Vacic, J. M. Criscione, N. K. Rajan, E. Stern, T. M. Fahmy, M. A. Reed, *J. Am. Chem. Soc.* **2011**, *133*, 13886.
[43] N. Nakatsuka, K.-A. Yang, J. M. Abendroth, K. M. Cheung, X. Xu, H. Yang, C. Zhao, B. Zhu, Y. S. Rim, Y. Yang, P. S. Weiss, M. N. Stojanović, A. M. Andrews, *Science* **2018**, *362*, 319.
[44] D. T. Miyamoto, K. W. Mouw, F. Y. Feng, W. U. Shipley, J. A. Efstathiou, *Lancet Oncol.* **2018**, *19*, e683.
[45] D. Margel, M. Pevsner-Fischer, J. Baniel, O. Yossepowitch, I. R. Cohen, *Eur. Urol.* **2011**, *59*, 113.
[46] S. L. Wood, M. A. Knowles, D. Thompson, P. J. Selby, R. E. Banks, *Nat. Rev. Urol.* **2013**, *10*, 206.
[47] M. Frantzi, A. Latosinska, L. Fluhe, M. C. Hupe, E. Critselis, M. W. Kramer, A. S. Merseburger, H. Mischak, A. Vlahou, *Nat. Rev. Urol.* **2015**, *12*, 317.
[48] M. Babjuk, M. Burger, E. M. Comperat, P. Gontero, A. H. Mostafid, J. Palou, B. W. G. van Rhijn, M. Roupret, S. F. Shariat, R. Sylvester, R. Zigeuner, O. Capoun, D. Cohen, J. L. D. Escrig, V. Hernandez, B. Peyronnet, T. Seisen, V. Soukup, *Eur. Urol.* **2019**, *76*, 639.
[49] S. Bravaccini, V. Casadio, R. Gunelli, L. Bucchi, W. Zoli, D. Amadori, R. Silvestrini, D. Calistri, *Ann. Oncol.* **2011**, *22*, 2294.
[50] M. B. Amin, S. C. Smith, V. E. Reuter, J. I. Epstein, D. J. Grignon, D. E. Hansel, O. Lin, J. K. Mckenney, R. Montironi, G. P. Paner, H. A. Al-Ahmadie, F. Algaba, S. Ali, I. Alvarado-Cabrero, L. Bubendorf, L. Cheng, J. C. Cheville, G. Kristiansen, R. J. Cote, B. Delahunt, J. N. Eble, E. M. Genega, C. Gulmann, A. Hartmann, C. Langner, A. Lopez-Beltran, C. Magi-Galluzzi, J. Merce, G. J. Netto, E. Oliva, et al., *Mod. Pathol.* **2015**, *28*, 612.
[51] B. Wang, C. Z. Zhao, Z. Q. Wang, K. A. Yang, X. B. Cheng, W. F. Liu, W. Z. Yu, S. Y. Lin, Y. C. Zhao, K. M. Cheung, H. S. Lin, H. Hojaiji, S. Emaminejad, *Sci. Adv.* **2022**, *8*, eabk0967.
[52] Y. Zhao, Z. Wang, G. Xu, L. Cai, T. H. Han, A. Zhang, Q. Wu, R. Wang, T. Huang, P. Cheng, S. Y. Chang, D. Bao, Z. Zhao, M. Wang, Y. Huang, Y. Yang, *Adv. Funct. Mater.* **2020**, *30*, 2003285.
[53] D. P. Kingma, J. Ba, *arXiv: 1412.6980*, **2015**.
[54] F. Pedregosa, G. Varoquaux, A. Gramfort, V. Michel, B. Thirion, O. Grisel, M. Blondel, P. Prettenhofer, R. Weiss, V. Dubourg, J. Vanderplas, A. Passos, D. Cournapeau, M. Brucher, M. Perrot, E. Duchesnay, *J. Mach. Learn. Res.* **2011**, *12*, 2825.